Journal of Materials Chemistry A

Accepted Manuscript

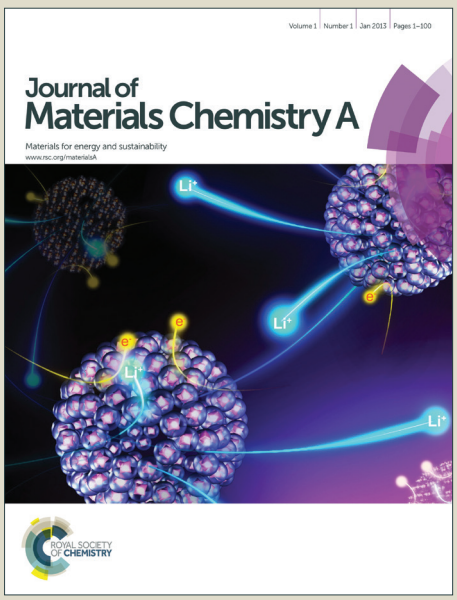

ROYAL SOCIETY OF CHEMISTRY

www.rsc.org/materialsA

Journal of
Materials Chemistry A

ARTICLE

Electrocatalytic hydrogen evolution using graphitic carbon nitride coupled with nanoporous graphene co-doped by S and Se

Received 00th January 20xx,
Accepted 00th January 20xx

DOI: 10.1039/x0xx00000x

www.rsc.org/

S.S. Shinde, Abdul Sami, and Jung-Ho Lee*

Electrocatalytic hydrogen evolution using non-precious metals or metal-free catalysts is critically necessary because platinum-based electrocatalysts are greatly limited in scalable commercialization of hydrogen generation due to their high cost. Here, we report the facile synthesis of metal-free hybrid catalysts, in which the graphitic carbon nitride (g-C_3N_4) is coupled with nanoporous graphene doped by S and Se. The S and Se co-doped hybrid catalyst (g-C_3N_4@S-Se-pGr) reveals superior electrocatalytic performances, including an exchange current density of 6.27×10^{-6} A cm^{-2}, on-set potential of 0.092 V, Tafel slope of 86 mV/dec, adsorption free energy of -0.13 eV, and long-term stability comparable to those of commercial Pt/C catalysts. Volcano plots showing the hydrogen evolution activity versus adsorption free energy are also compatible with those of the conventional metal catalysts. Our strategy has the potential to allow a new paradigm for the development of high-performance metal-free electrocatalyst for energy conversion devices.

Introduction

Hydrogen is being vigorously pursued as a future energy carrier in the transition from the current hydrocarbon economy. There have been increasing efforts to develop efficient, stable, and low-cost electrocatalysts in the past decades.[1] Among the candidates, Pt or Pt-based carbon catalysts have shown superior electrocatalytic performance, including extremely high exchange current densities and small Tafel slopes in the hydrogen evolution reaction (HER);[2] however, the high cost of platinum catalysts and the slow HER kinetics at the cathode are major hurdles preventing scalable commercialization.[3] Intensive efforts have therefore been made to replace Pt-based catalysts with various transition metals such as Cu, Ti, Mo, Co, Ni, Fe, and their derivatives.[4] However, their inherent susceptibility to corrosion and oxidation greatly limit the effectiveness for acidic electrolysis based upon proton-exchange membranes.[5] Therefore, high-performance metal-free catalysts would be a reasonable solution for successful commercialization of molecular hydrogen as a clean energy source instead of fossil fuels.[6]

It is also a challenging and exciting task to develop active catalysts that preferably expose a large fraction of the catalytically reactive sites. Since carbon-based catalysts and their derivatives are potential candidates for replacement of Pt catalysts, the graphene (Gr) family is emerging as an efficient, reliable, and sustainable alternative for HER owing to their highly conductive and excellent mechanical properties. Given the significant importance of edge sites in electrocatalysis, precise adjustment of porosity on the graphene surface is technically challenging; moreover, it would be beneficial to develop nanoporous graphene without metal contamination or extensive damage to the pristine graphene matrix. One promising candidate for electrocatalytic applications of graphene is the oxygen reduction/evolution occurring at the cathode of fuel cells and metal-air batteries, in which the electrocatalysts adopting metal-free graphene are considered a possible alternative with respect to the state-of-the-art Pt catalysts due to low cost, fuel tolerance, and long-term durability.[7]

To date, however, the overall electrocatalytic HER performance (i.e., exchange current density, on-set potential, and Tafel value) of metal-free catalysts based on the graphene family are still subject to debate. The origin of graphene activity toward HER and the doping effect of non-metallic hetero-atoms remain unclear. Here we report the first successful synthesis of molecular designed, metal-free catalysts synthesized by coupling a graphitic carbon nitride (g-C_3N_4) with graphene doped by S, Se, or S-Se. These graphitic carbon nitride hybrids (g-C_3N_4@S-Se-pGr, for instance, co-doped by S and Se) possess unique chemical and electronic properties for HER, which are comparable to those of well-developed conventional metallic catalysts such as Pt/C and MoS_2. In our *in-situ* process, nanoporous graphene (pGr) is prepared first by removing graphene quantum dots (GQDs) using chemically-assisted oxidative etching. A nanoporous graphene surface enriched with broken carbon bonds is capable of acting as an active site for doping non-metal atoms along the pore edges. The interesting feature we observe is a synergistic effect of the graphitic carbon nitride hybrids, in which the g-C_3N_4 provides highly active hydrogen adsorption sites, while the S-Se-co-doped porous graphene facilitates the electron-transfer process for proton reduction. The robust stability of our metal-free catalysts is observed over a wide pH range, and the HER mechanism is estimated from the Volmer–

Department of Materials and Chemical Engineering, Hanyang University, Ansan, Kyunggido, 426-791, Korea. E-mail: jungho@hanyang.ac.kr, Phone: +82-31-400-5278, Fax: +82-31-419-7203

Electronic Supplementary Information (ESI) available: [details of any supplementary information available should be included here]. See DOI: 10.1039/x0xx00000x

Heyrovsky and Volmer–Tafel reactions. Our approach adds credence to the vast potential of molecular designed, metal-free hybrid catalysts for highly efficient electrocatalytic HER.

Experimental

Preparation of graphene oxide (GO)

Briefly, graphite powder (3.0 g) was added to concentrated H_2SO_4 (70 mL) under stirring in an ice bath. Under vigorous agitation, $KMnO_4$ (9.0 g) was added slowly to keep the temperature of the suspension lower than 20 °C. The reaction system was successively transferred to a 40 °C oil bath and vigorously stirred for about 30 min. Then, 150 mL water was added, and the solution was stirred for 15 min at 95 °C. An additional 500 mL water was added and followed by a slow addition of 15 mL H_2O_2 (30%). The mixture was filtered and washed with a 1:10 HCl aqueous solution to remove metal ions. The mixture was subjected to centrifugation at 12000 rpm, and the supernatant solution was decanted away. The remaining material was subjected to multiple washings with water, ethanol, acetone, and polyether in sequence and conserved for further use.

Preparation of graphene (Gr) from graphene oxide (GO)

Graphene was prepared through the pyrolysis of GO at high temperature in an inert (N_2) atmosphere. Briefly, GO was loaded into an alumina boat, which was placed in a quartz tube. The tube was kept in a tubular furnace under an inert atmosphere by purging N_2 and maintaining a flow rate of 0.5 sccm. Subsequently, the temperature of the furnace was increased to 900 °C and maintained for 3 h. The furnace was then allowed to cool to room temperature after pyrolysis with N_2 flow. The pyrolyzed product was then preserved for further studies.

Preparation of nano-porous graphene (pGr) and functionalization of OH group

The pGr and functionalized product were prepared simultaneously by H_2O_2 oxidation of Gr. Briefly, 1 g of Gr was dispersed in 500 ml of H_2O_2 (30 %) with the aid of sonication for 60 hr at 70 °C. The resulting mixture was filtered using filter paper with a pore size of 0.45 µm (Rankem Chemicals), and the filtrate was lyophilized for 3 h and preserved for further analyses.

Synthesis of x-graphene (x-pGr)

S and/or Se porous graphene were prepared by direct annealing of lyophilized pGr with sulfur and selenium powder at a mass ratio of 1:1, 1:1, and 1:0.5:0.5, respectively. Briefly, pGr and respective precursor elements were ultrasonically dispersed in ethanol for about 30 min. The resulting suspension was concentrated by rotary evaporation and followed by lyophilization. The respective mixtures were then annealed at 900 °C for 3 h under N_2 and allowed to cool to room temperature. These samples were used for further experimentation.

Synthesis of g-C_3N_4@x-pGr

The g-C_3N_4@x-pGr hybrid was synthesized by mixing dicyandiamide (DCDA) with x-pGr (in 1:3 mass ratio). Briefly, x-pGr and DCDA were ultrasonically dispersed in ethanol for about 30 min, and then the mixture was concentrated by rotary evaporation followed by lyophilization. The mixture was then annealed at 600 °C for 4 h at a heating rate of 10 °C min^{-1}. Finally, these samples were used to determine electrocatalytic HER performance.

Chemical characterization

Transmission electron microscopy (TEM) images were obtained using a JEOL JEM-2100F machine operated at 200 kV. The EDS map was obtained using a TESCAN (MIRA3). The X-ray photoelectron spectra (XPS) were collected by a high-resolution and high-sensitivity hemispherical electron analyzer with nine-channel electron multipliers (VG SCIENTA (R 3000)). The incident radiation was monochromatic Al Ka X-rays (1,486.6 eV) at 225 W (15 kV, 15 mA). Nitrogen adsorption−desorption isotherms were measured on an AUTOSORB-1-MP surface analyzer. Raman spectra were produced on RM 1000 (Ranishaw, UK) spectrometer.

Electrochemical characterization

Glassy carbon (GC) electrodes (3 mm diameter, CH Instrument Inc.) were polished with 0.05 and 0.3 µm alumina slurry (CH Instrument Inc.), subsequently rinsed with ultrapure water and ethanol, and dried under a gentle nitrogen stream. To prepare the working electrode, all of the carbon catalyst (1 mg/ml) was ultrasonically dispersed in distilled water (Milli-Q) containing 0.1 wt% of Nafion. Then 20 µL of the resulting suspension was dropped onto the GC surface and dried at room temperature, producing a working electrode. The Pt wire acted as the counter electrode, and Ag/AgCl in 4M AgCl–KCl solution was the reference electrode. Electrochemical impedance spectroscopy (EIS) was performed in the frequency range from 0.1 Hz to 2 KHz with a 5 mV amplitude at a bias potential of 0.2 V. All potentials were referenced to that of a reversible hydrogen electrode (RHE) by adding a value of (0.205 + 0.059 × pH) V. A flow of N_2 was maintained in the electrolyte during the experiment to remove dissolved oxygen (the electrolyte was purged for 30 min by N_2 flow before the experiment).

Results and discussion

The simple H_2O_2 oxidation of graphene (Gr) was used to prepare nanoporous graphene (pGr) at 70 °C through the removal of graphene quantum dots (GQDs), in which strongly oxidized free radicals such as $OH^{\bullet}$ and $HO_2^{\bullet}$ were produced to induce hydroxyl ($OH^{\bullet}$) functionalities on the sp^2 carbon (C=C) along the pore openings. To obtain a doped graphene matrix (x-pGr), pGr was used as a substrate for the effective active sites doped by non-metallic elements (S, Se, S-Se). For strong chemical adhesion, g-C_3N_4 was grown directly on the chemically exfoliated x-pGr surface. Concomitantly, x-pGr was thermally reduced by gaseous nitrogen molecules that were released during the polycondensation of dicyandiamide (DCDA) into melem units. As a result, the g-C_3N_4@x-pGr hybrid was formed (see Fig. 1a). A detailed experimental procedure is described in the experimental. Figs. 1 (b-d) contain the transmission electron microscopy (TEM) images showing Gr and pGr, in which the presence of nanoscale pores is revealed on the H_2O_2-treated graphene surface (pGr, panels c and d) in contrast to the pure Gr (panel b). Detached GQDs were resolved in sizes of 3~5

nm (panel e) with high crystallinity. A lattice spacing of 0.242 nm is shown with a (1120) lattice fringe of graphene. Pore sizes of 3~5 nm agree well with the average GQD sizes, highlighting the detachment of these GQDs from the Gr surface (Also confirmed from size distribution map as shown in Fig. S1). Since the edge-site generation in graphene is crucial for producing the maximum number of catalytically active sites, the removal of GQDs from the graphene 2D-matrix is one of the major solutions to effectively achieve edge sites for doping heteroatoms. Zigzag-shaped edges in graphene were reported to offer distinctive electronic or magnetic properties.[8] The evolution of zigzag orientations is denoted in the two-dimensional fast Fourier transform (2D-FFT) pattern (see red arrows in the inset of Fig. 1e).

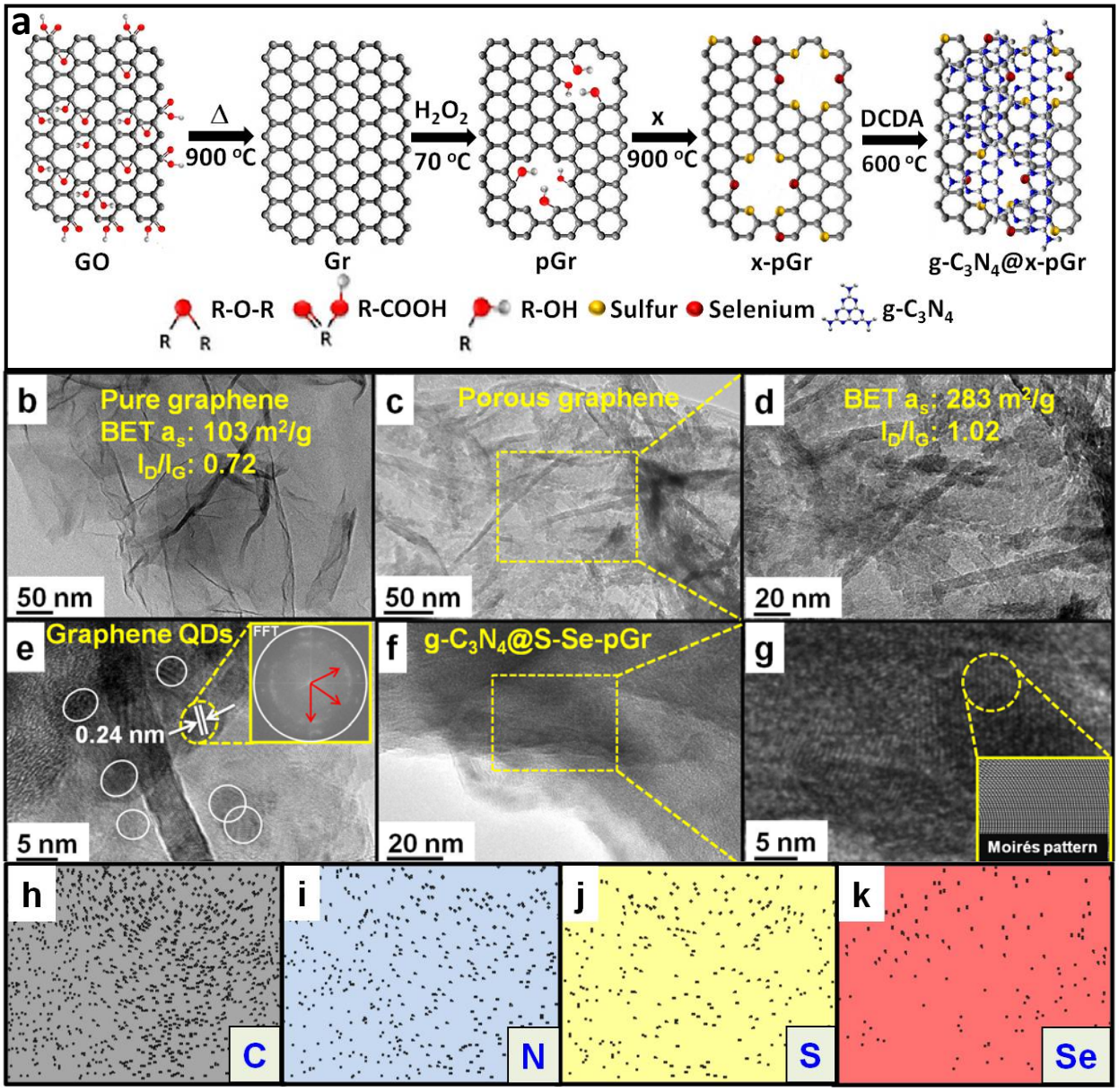

Fig. 1 (a) Schematic representation of the growth of g-C_3N_4@x-pGr hybrid graphene (x= S, Se, S-Se). TEM images of (b) pure graphene and (c-d) nanoporous graphene (different magnification). The inset values represent the I_D/I_G ratios and the specific surface areas obtained from Raman spectra and nitrogen adsorption isotherms, respectively. Images (b-c) are the TEM images of pGr with nano-pores, and the characteristic features of the graphene surface are clearly visible on this image, while the characteristic features of the pores are not present in the case of pure graphene. (e) Graphene quantum dots (GQDs), inset is the 2D FFT and schematic illustration showing the orientation of the hexagonal graphene network and the relative zigzag directions. (f-g) TEM images of typical g-C_3N_4@S-Se-pGr catalyst, the inset shows a schematic Moirés pattern that is commonly observed in prepared hybrids due to stacking layers, (h-k) EDS mapping of individual elements (C, N, S, Se).

Nitrogen-adsorption studies also clarify that the surface area of porous graphene (283 $m^2\ g^{-1}$) was enhanced upon H_2O_2 oxidation in comparison to that of pure graphene (103 $m^2\ g^{-1}$) (see Figs. S2a-b, ESI). Pore-size distribution (inset in Fig. S2b) indicates a nanoporous morphology on the graphene surface. Similarly, the Raman intensity ratio (I_D/I_G) comparing the defect-induced band and the graphitic carbon band increased from graphene (~0.72) to porous graphene (~1.02) (Fig. S3a, ESI). The graphitic carbon nitride hybrid, i.e., g-C_3N_4@S-Se-pGr, shows the Moiré-fringed two-dimensional sheets

(inset of panel g), in which a multilayered structure consists of a g-C_3N_4 matrix stacked on the S-Se-pGr sheet (panels f and g).

Elemental analysis of the g-C_3N_4@S-Se-pGr hybrid spatially visualizes the EDS mapping (panels h-k). Graphitic sp^2-carbon species are observed to be well-distributed over the entire sheet (panel h), whereas the co-doped S and Se species are likely confined to the specific defective sites (panels j and k). This is similar to the partially covered g-C_3N_4 regions, as clarified in the X-ray photoelectron spectroscopy (XPS) evidence (i.e., $\pi^*_{C\text{-}N\text{-}C}$ peak at 288.7 eV in Fig. 2a). The presence of defective species might be attributed to the low-coordinated carbon atoms originating from the breakage of N–3C bridging bonds (see N 1s core-level in Fig. 2b) at the edge of the g-C_3N_4 sheets, due to strong interaction between the g-C_3N_4 and S-Se-pGr substrate. Atomic concentrations of S and Se are estimated to be 2~5 at%, which is also consistent with the XPS results of Figs. S4b-c (ESI).

Raman spectroscopy characterized the graphitic nature of the Gr-catalysts (Figs. S3 a-b, ESI). The peak around 1582–1584 cm^{-1} reflects the presence of graphitic carbon (G-band) through the E_{2g} vibrational mode of C–C bond stretching (sp^2 carbon domains), while the peak at 1350–1355 cm^{-1} represents the defective sites via the A_{1g} vibrational mode of C.[9] The G peak in S- and/or -Se-doped pGr hybrids were found to red-shift to 1582 cm^{-1} in comparison to 1589 cm^{-1} of the pristine graphene, implying the formation of hybrids.[10] If the intensity of the defect-induced D-band is stronger than that of the G-band in certain samples, it is reasonable to conclude that a relatively large number of graphitic defects have been exposed and can serve as redox active sites. The amount of defects present in the Gr-samples is estimated by the intensity ratio of I_D/I_G, which is strongly correlated with the electrical conductivity of each sample. Since the intensity ratios of all our samples likely converge to a close distribution (I_D/I_G = 0.99~1.04) of defect concentration, it is plausible that a major difference in the electrocatalytic HER activities is dominated by the extra doping effect rather than by the physicochemically different characteristics of the samples. Doping of S (or Se) normally prefers the defect sites of a Gr-matrix, without the need for generating further defect sites through the breakage of C–C bonds in a sp^2-carbon lattice.

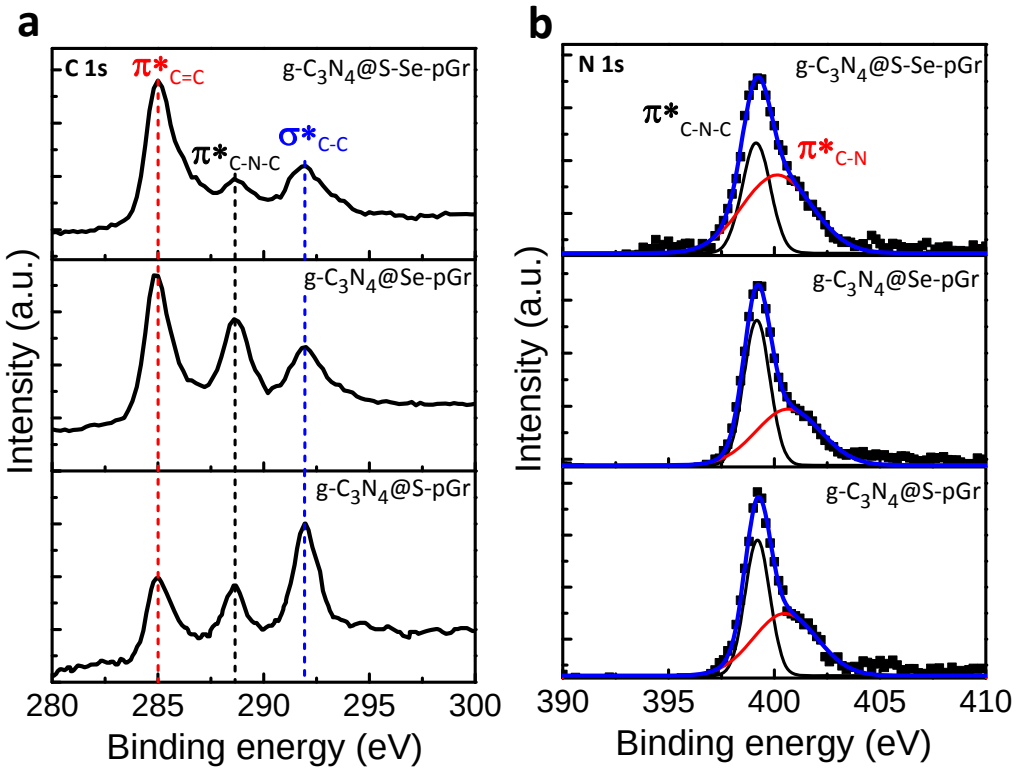

Fig. 2 Chemical analysis of g-C_3N_4@x-pGr. High-resolution XPS spectra of (a) Carbon, (b) Nitrogen, (Deconvoluted peaks show two types of nitrogen species; the black peak refers to pyrrolic and the red peak refers to graphitic nitrogen).

Peak-deconvoluted, high-resolution XPS further resolved the nature of doping (see Fig. S4, ESI), as reported in a previous work.[11] Heteroatoms are known to chemically substitute the edge- or central-carbon atoms in the Gr-matrix, finally yielding 13 different species in (or out of) a graphene basal plane.[12] All samples were ultrasonically dispersed in ethanol in order to distinguish whether the S (or Se) signal arises from the physical adsorption of dopant or from the covalent C-S (or C-Se) bonding. XPS results support a strong covalent binding between C-S (or C-Se) because no evidence of change is detected for the S (or Se) level upon sonication. Moreover, previous investigations have demonstrated that the C 1s peak of sp^2 carbon becomes asymmetrically broadened toward the high-energy side as the number of functional groups increases.[13] For the g-C_3N_4@x-pGr, Fig. 2a shows that the C 1s peaks (corresponding to sp^2 carbon atoms) normally blue-shift to binding energies ($\pi^*_{C=C}$ ~285 eV) higher than that of pristine graphene (284.2 eV) (see Fig. S4a, ESI), and their full-width at half-maximum (FWHM) at 285 eV are increased by incorporating S and/or Se.

Characteristic C 1s core-level peaks, i.e., two π* edges (285, 288.7 eV) and one σ* edge (291.9 eV), correspond to the graphitic, defective, and sp^3 carbon species, respectively.[14] These π* and σ* resonances also represent the core-level electron transitions between unoccupied antibonding π* and σ* orbitals. The σ* excitation indicates the presence of new sp^3 carbon species formed by nanoscale g-C_3N_4 domains grown on S and/or -Se-pGr surfaces, supporting the idea that the chemical coupling between g-C_3N_4, S-Se-pGr, C-S-C (Fig. S4b, ESI), and C-Se-S (Fig. S4c, ESI) bindings are induced during the thermal exfoliation process. The N 1s core-level peak in Fig. 2b consists of two typical π* resonances fitted at 399.1 and 400.6 eV, which correspond to the aromatic C–N–C coordination in one tri-s-triazine heteroring (π^*_{C-N-C}) and the N–3C bridging among three tri-s-triazine moieties (π^*_{C-N}), respectively.[15] These two π* resonances also represent the C-N bonds in the form of pyrrolic nitrogen (399.1 eV) and graphitic (400.6 eV) nitrogen, respectively. The co-existence of pyrrolic/graphitic nitrogen types is capable of generating more active sites for higher HER activity, while providing an effective chemical interconnection between g-C_3N_4 and x-pGr for rapid electron transfer. Our XPS results coupled with Raman spectroscopy strongly support the assumption that sulfur and selenium atoms have been chemically substituted into a graphene framework via covalent binding.

Electrocatalytic activities of the g-C_3N_4 chemically coupled with S- and/or Se-doped porous graphene were investigated in both acidic (0.5 M H_2SO_4) and alkaline (0.1 M KOH) aqueous solutions using the linear sweep voltammetry (LSV) methods at constant active mass loading. Figs. 3 (a-d) show the HER polarization curves and the corresponding Tafel plots of various electrocatalysts in 0.5 M H_2SO_4 and 0.1 M KOH solutions. Graphitic carbon nitride has a negligible electrocatalytic activity compared to the doped and coupled hybrids. Graphitic carbon nitride with S-Se-pGr hybrid catalyst (i.e., g-C_3N_4@S-Se-pGr) shows the lowest overpotential of -300 mV to achieve 10 mA/cm^2 current density of HER, along with a Tafel slope of 86 mV dec^{-1} in 0.5 M H_2SO_4 (Tables S1 and S2, ESI), beyond which the cathodic current increased rapidly under more negative potentials. The exchange current density (i_0) of HER for g-C_3N_4@S-Se-pGr was calculated to be 6.27×10^{-6} A cm^{-2} through the extrapolation method from the Tafel plot (Fig. 3e). Representative HER activities such as electrochemical active surface area, exchange current density, catalyst loading, and on-set potential values indicate that the overall performance of g-C_3N_4@S-Se-pGr was comparable or even better than those of traditional metallic catalysts (bulk Au, Mo, and MoS_2 alloy) and metal-free catalysts (graphene, doped graphene, C_3N_4 and C_3N_4/graphene).[16] A current density measurement reveals a clear trend in which electrocatalytic activity scales with the electrochemically active surface area and the amount of substituted heteroatoms. From the comparison of normalized exchange current densities between g-C_3N_4@S-Se-pGr and the metallic catalysts (see Figs. S5a-b and Tables S3-4 ESI for detailed normalization procedure), the graphene hybrid materials were shown to have vast potential for replacing metallic catalysts via nanostructure engineering.

The chemical coupling effect on the catalytic activity of hybrid graphene is further confirmed by Tafel plots (Figs. 3 b and d). Apart from the doping effect, the chemical coupling/interaction also remarkably influence the catalytic activity of doped graphene because, it introduce more structure defect sites and hence change its chemical activity. The determination and interpretation of Tafel slopes are important for elucidation of the elementary steps involved. The g-C_3N_4@S-Se-pGr has much better catalytic activity with regard to onset potential and Tafel slope among the grown samples. A Tafel slope represents an inherent characteristic of a catalyst that is determined by the rate-limiting step of HER. We observed that the Tafel slope varied in the range of 84-93 mV dec^{-1} for coupled hybrid catalysts and in that of 105-124 mV dec^{-1} for simply doped graphenes (Table S1, ESI). Generally, three possible reaction steps for HER in acidic electrolytes have been suggested. It includes a primary discharge step (Volmer reaction, Tafel slope ~120 mV/dec), an electrochemical desorption step (Heyrovsky reaction, Tafel slope ~40 mV/dec) and recombination step (Tafel reaction, Tafel slope ~30 mV/dec) respectively.[17] From this, it concludes that an initial proton adsorption (Volmer reaction) is the rate-determining step of the whole HER process. Such actions could be elucidated by the free energy analysis that of g-C_3N_4@S-Se-pGr hybrid catalyst shows a slightly negative free energy value closer to a Pt value with an enhanced adsorbing capability for hydrogen. Usually, traditional metallic electrocatalysts are active under either acidic or basic conditions,[4f,18] but prepared graphene-based hybrid catalysts showed favourable HER performance in a wide range of pH values. Metal-free hybrid catalysts (Fig. 3c) show lower HER activity in alkaline (i.e., KOH) solution than in acidic solution, but demonstrate a similar tendency of activity (i.e., variation in overpotential, i_0, with S- and/or Se-doped hybrid catalysts) to realize the dopant effect. The distinction may occur due to the different HER mechanisms under the two conditions, i.e., there might be an additional water dissociation step when using the alkaline solution, and these catalysts are critical to assist this step, resulting in a relatively high energy barrier in the HER process.

A synergistic coupling effect in g-C_3N_4@x-pGr was quantitatively evaluated in terms of the exchange current density (i_0) derived from the Tafel plots (Fig. 3e). The g-C_3N_4@S-Se-pGr hybrid catalyst showed the highest values of i_0 (6.27×10^{-6} and 5.58×10^{-7} A cm^{-2} in H_2SO_4 and KOH solutions, respectively), in which the resulting exchange current density was lower in an alkaline solution. The obtained current density of g-C_3N_4@S-Se-pGr is 6.27×10^{-6} A cm^{-2} higher than those of g-C_3N_4@S-pGr and g-C_3N_4@Se-pGr. Hybrid metal-free catalysts exhibited the onset for HER at overpotentials of approximately 92−162 mV, in contrast to the 330-417 mV for simply doped active sites. These values are comparable to the best dichalcogenide catalysts and even better than recently developed nanoporous graphite–C_3N_4 composites and N, P, S, N-P doped carbon materials (Table S1).[16,19] Therefore, g-C_3N_4@S-Se-pGr might be one of the best metal-free catalysts reported to date in HER. A gradual decrease in the onset potentials from S-pGr to g-C_3N_4@S-Se-pGr confirms the enhancement in HER. Resistance to crossover effects (i.e., chemical coupling/interactions) and the stability of the

catalyst materials are important considerations for practical applications. Although the covalent bonding between g-C_3N_4 and S-Se-pGr was anticipated to form a strong molecular structure, we practically examined the long-term stability over 1000 cycles (Fig. 3f). As a result, we observe the negligible loss of cathodic current at the end of 1000 cycles, ensuring the robust stability of g-C_3N_4@S-Se-pGr catalysts in both acidic and alkaline solutions for a sustainable HER performance.

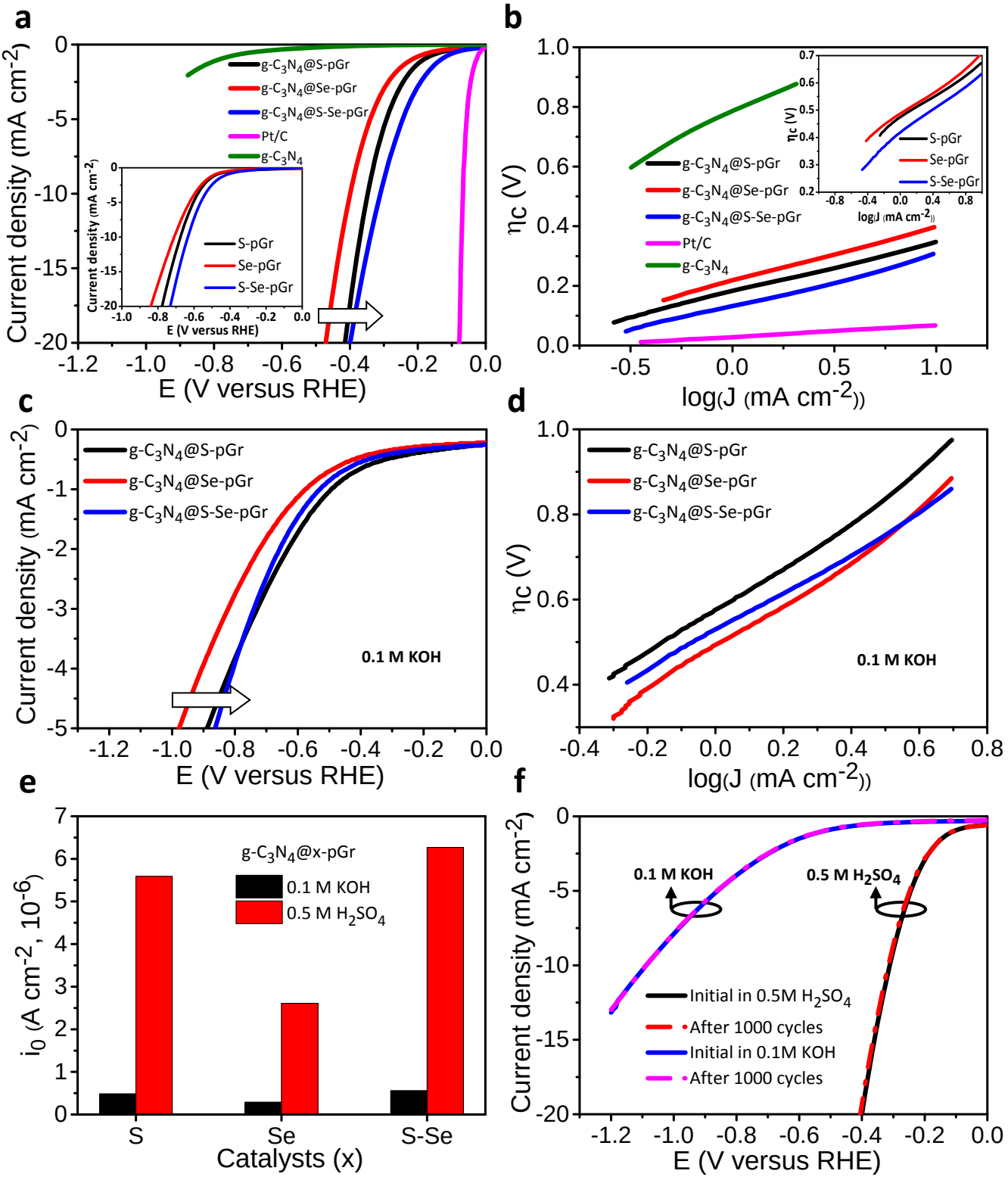

Fig. 3 HER polarization curves and the corresponding Tafel plots of three different metal-free hybrid electrocatalysts in (a-b) 0.5 M H_2SO_4 and (c-d) 0.1 M KOH. (e) Comparison of calculated i_0 values for different metal-free catalysts in 0.5 M H_2SO_4 (red colored bars) and 0.1 M KOH (black colored bars) solutions, (f) Polarization curves for g-C_3N_4@S-Se-pGr hybrid before and after 1,000 potential sweeps under acidic and basic conditions.

Journal of
Materials Chemistry A

ARTICLE

Compared to simply doped graphenes, these improved features of metal-free hybrid catalysts are due not only to the increase in active sites, but also to faster electron transfer through a larger number of conductive paths generated by carbon nitride (a synergistic effect increasing the capacities of proton adsorption and reduction). The chemical and electrical coupling to the graphene in an interconnected conducting network afforded rapid electron transport from the weaker-conducting g-C_3N_4 to the electrodes. To analyze this effect, we have performed the electrochemical impedance measurements at 200 mV, as shown in Fig. 4a; inset shows the corresponding equivalent circuit. Apparently lower Faradaic resistances of the hybrid catalysts imply that the enhanced electrocatalytic performance of g-C_3N_4@S-Se-pGr is originated from the higher electrical conductivity and the chemical interaction between g-C_3N_4 and S-Se-pGr. Introduction of g-C_3N_4 into S-Se-pGr might be effective to induce the defect-mediated π-conjugations at the edges of carbon materials, producing faster electron transfer. The g-C_3N_4 coupled with S and Se atoms effectively redistributes the spin and charge densities in order to induce a large number of active carbon sites, in which the spin density was reported to be more crucial than the atomic charges for determining the catalytic active sites from the density functional theory (DFT) calculation.[20]

In Fig. 4b, the activation energies (E_a) of 0.42-0.47 eV for HER were plotted via the Tafel reaction of hybrid metal-free catalysts. The change in activation energies is closely related to the variation in proton coverage on the catalyst surfaces. Volcano plots reveal the quantitative relation between the measured electrochemical activities and the free energies of hydrogen adsorption. Fig. 4c shows the volcano plots of exchange current densities (i_0) experimentally measured as a function of free energy (ΔG_H*) for newly developed g-C_3N_4@x-pGr (pink-shaded circle) hybrid metal-free catalysts and common metal catalysts, as previously reported.[4b,21] Catalytic performance is determined by the position of the i_0 vs. ΔG_H* relative to the volcano peak position, in which the closer positions (i.e., toward a zero free energy in a volcano plot) are recommended for better catalysts.[22] Our metal-free catalysts are positioned reasonably in the volcano plot, which confirms a better activity than those of the other metallic electrocatalysts previously reported.[23]

Fig. 4d shows the HER free energy diagram of g-C_3N_4@x-pGr in order to study a synergistic effect in electrocatalytic activity. In general, the reaction pathway of HER is categorized into three-states; the initial state of $H^+ + e^-$, an intermediate state of adsorbed H*, and the final state of ½H_2.[4b,21] Generally, in the case of well-developed metallic catalysts, HER activity is strongly dependent on the adsorption free-energy. If the free energy of the catalyst is positive, then the intermediate H* formation is the rate-determining step of the HER; when free energy is negative, desorption of H* to form H_2 is the rate-determining step.[22] Compared to the highly efficient metallic Pt catalysts of near-zero (-0.09 eV) free energy,[4b] the g-C_3N_4@S-Se-pGr catalyst records a free energy of -0.13 eV. In contrast to hybrid catalysts, most of the simply doped graphenes have shown weaker electrocatalytic activities due to much higher positive free energies in the range of 0.57-0.65 eV, which renders proton transfer more difficult because hydrogen becomes more unstable on the surface. Efficient transfer of electrons from the S-Se-pGr surface to catalytically active g-C_3N_4 domains causes a quick reduction of the adsorbed H* into molecular hydrogen. High HER activities of the metal-free hybrid catalyst stem from the synergistic feature between chemical and electronic couplings.

The HER mechanism on the metal surfaces has been studied in detail using the kinetics of the Tafel reaction,[22] it is inconclusive regarding metal-free catalysts. Thus, we have attempted to explain the HER mechanisms using Volmer–Heyrovsky and Volmer–Tafel reactions.[2,24] The possible reaction pathways for g-C_3N_4@S-Se-pGr at the equilibrium potential are illustrated on a free energy diagram presented in Figs. 4 (e-f). Here we considered only solid lines by making supposition that there were no extra energy barriers related to the whole HER process. Under the measured on-set potential (0.092 V vs RHE from the polarization curve), the free energy of the reactant and intermediate states shift upward as compared to the equilibrium potential (Fig. 4f). This shift in energy is overcome at higher overpotential, i.e., at 0.3 V, the free energy of the second and third reaction steps remains same (Volmer-Tafel HER pathway). Hence, the selectivity of pathway on g-C_3N_4@S-Se-pGr is potential-dependent. At low overpotential, the most probable mechanism is the Volmer–Heyrovsky (rate limiting step - electrochemical desorption); at high overpotential is the Volmer–Tafel mechanism (rate limiting step - recombination). Reduction in energy shift with increasing overpotential, indicates the first electron transfer step is no longer the rate-limiting step for the overall reaction, i.e., the whole HER process is activated. The previously reported potential-dependent barrier values of the Pt surface[4c] are depicted as dashed lines in Figs. 4 (e-f). Here we considered that the g-C_3N_4@S-Se-pGr hold similar energy barriers to those on the Pt surface for each reaction step. Compared with the observed overpotential and Tafel slope, the Volmer–Tafel mechanism is more suitable than Volmer–Heyrovsky in the g-C_3N_4@S-Se-pGr hybrid catalyst.

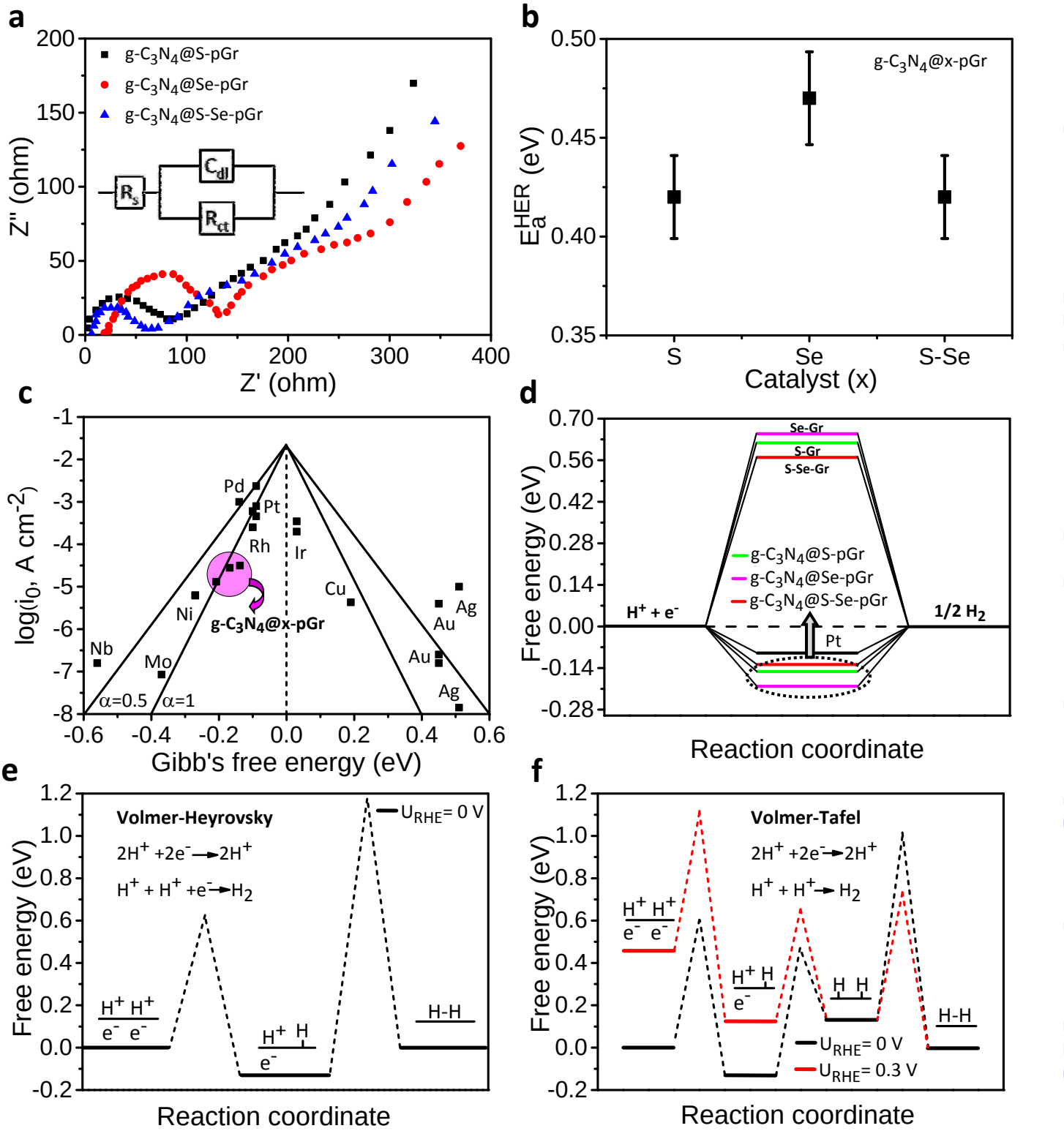

Fig. 4 (a) Electrochemical impedance spectroscopy data for different metal-free catalysts in 0.5 M H_2SO_4; data were collected for the electrodes under HER overpotential = 200 mV; frequency range = 20 kHz- 2MHz; inset shows the corresponding equivalent circuit. (b) Activation barrier, E_a, for HER via the Tafel reaction for different hybrid metal-free catalysts, (c) Volcano plots of experimentally measured exchange current i_0 as a function of Gibb's free energy (ΔG_H*) for newly developed g-C_3N_4@x-pGr (pink shaded area) and common metal catalysts (Refs. 4b, 22). The two curved lines correspond to the transfer coefficients α = 0.5 and 1.0 respectively. (d) The calculated free energy diagram for HER at the equilibrium potential (U_{RHE} = 0). (e) Reaction pathways of HER on g-C_3N_4@S-Se-pGr according to the Volmer–Heyrovsky reaction and (f) Volmer–Tafel reaction. Dashed lines are previously reported energy barriers for each reaction step on the Pt surface.[4c] (The H^+/e^- and H-H are the intermediates states of adsorption free energies of HER.)

Journal of
Materials Chemistry A

ARTICLE

Conclusions

In summary, this work reports the first design and fabrication of coupled graphitic carbon nitride (g-C_3N_4) with S- and/or Se-doped porous graphene hybrid catalysts through a facile, economical, and scalable approach. The novel material studied exhibit an excellent catalytic activity with minimum catalyst loading compared to metal and metal-free catalysts, which makes it an ideal candidate for the next generation of HER catalysts. The highest HER performance of the g-C_3N_4@S-Se-pGr catalyst, an exchange current density of 6.27×10^{-6} A cm^{-2}, on-set potential of 0.092 V, Tafel slope of 86 mV/dec and adsorption free energy of -0.13 eV, revealed the extraordinary intrinsic features with chemical and electronic coupling, which synergistically promotes proton adsorption and reduction kinetics. The resulting catalyst also showed full tolerance and excellent stability during long-term cycling in acidic and alkaline environments. These findings confirm that the prepared metal-free hybrid catalysts are very suitable for the next generation of fuel cells and are capable for potential applications in other fields such as in batteries, photocatalysis, oxygen sensors, and water treatment.

Acknowledgements

This work was supported by a grant of the New & Renewable Energy Program of the Korea Institute of Energy Technology Evaluation and Planning (KETEP) (No. 20123010010160) funded by the Korean Ministry of Trade, Industry, and Energy. This work was also supported by a National Research Foundation of Korea (NRF) grant funded by the Korean government (MSIP) (No. 2011-0028604).

Notes and references

1 (a) S. Chen, J. Duan, Y. Tang, B. Jin, S. Zhang-Qiao, Nano Energy, 2015, **11,** 11; (b) J. Kibsgaard and T. F. Jaramillo, Ang. Chem., 2014, **53,** 14433; (c) W. Chen, S. Iyer, S. Iyer, K. Sasaki, C. Wang, Y. Zhu, J. Muckerman and E. Fujita, Energy Environ. Sci., 2013, **6,** 1818; (d) J. McKone, E. Warren, M. Bierman, S. Boettcher, B. Brunschwig, N. Lewis, H. Gray, Energy Environ. Sci., 2011, **4,** 3573

2 B.E. Conway, and B.V. Tilak, Electrochim. Acta., 2002, **47,** 3571.

3 (a) X. Chen, D. Wang, Z. Wang, P. Zhou, Z. Wu, F. Jiang, Chem. Commun., 2014, **50,** 11683; (b) Y.Y. Liang, Y.G. Li, H.L. Wang, J.G. Zhou, J. Wang, T. Regier, H.J. Dai, Nat. Mater., 2011, **10,** 780.

4 (a) M. Giovanni, H.L. Poh, A. Ambrosi, G. Zhao, Z. Sofer, F. Sanek, B. Khezri, R. D. Webster, M. Pumera, Nanoscale, 2012, **4,** 5002; (b) J. K. Nørskov, T. Bligaard, A. Logadottir, J. R. Kitchin, J. G. Chen, S. Pandelov, U. Stimmingc, J. Electrochem. Soc., 2005, **152,** J23; (c) E. Skulason, V. Tripkovic, M. Bjorketun, S. Gudmundsdottir, G. Karlberg, J. Rossmeisl, T. Bligaard, H. Jonsson, J. Nørskov, J. Phys. Chem. C, 2010, **114,** 18182; (d) A. B. Laursen, S. Kegnaes, S. Dahl and I. Chorkendorff, Energy Environ. Sci., 2012, **5,** 5577; (e) J. F. Xie, J. J. Zhang, S. Li, F. Grote, X. D. Zhang, H. Zhang, R. X. Wang, Y. Lei, B. Pan and Y. Xie, J. Am. Chem. Soc., 2013, **135,** 17881; (f) K. Christopher and R. Dimitrios, Energy Environ. Sci., 2012, **5,** 6640; (g) B. F. Cao, G. M. Veith, J. C. Neuefeind, R. R. Adzic and P. G. Khalifah, J. Am. Chem. Soc., 2013, **135,** 19186.

5 (a) Z. Huang, Z. Chen, Z. Chen, C. Lv, M.G. Humphrey, C. Zhang, Nano Energy, 2014, **9**, 373; (b) Y. Xu, M. Gao, Y. Zheng, J. Jiang, S. H. Yu, Angew. Chem., Int. Ed., 2013, **52,** 8546; (c) J. Ran, J. Zhang, J. Yu, M. Jaroniecc, S. Qiao, Chem. Soc. Rev., 2014, **43**, 7787.

6 (a) A. Bergmann, I. Zaharieva, H. Dau, P. Strasser, Energy Environ. Sci., 2013, **6,** 2745; (b) Z. Xing, Q. Liu, A.M. Asiri, X. Sun, Adv. Mater., 2014, **26**, 5702.

7 (a) U. Sim, T. Yang, J. Moon, J. An, J. Hwang, J. Seo, J. Lee, K. Kim, J. Lee, B. Hong, K. Nam, Energy Environ. Sci., 2013, **6,** 3658, (b) X. Li, J. Chen, X. Wang, J. Sun, M. Antonietti, J. Am. Chem. Soc., 2011, **133**, 8074, (c) C. Choi, H. Lim; M. Chung; J. Park; H. Shin; H. Kim; S. Woo, J. Am. Chem. Soc., 2014, **136,** 9070; (d) Y. G. Li, W. Zhou, H. L. Wang, L. M. Xie, Y. Y. Liang, F. Wei, J. C. Idrobo, S. J. Pennycook, H. J. Dai, Nat. Nanotechnol., 2012, **7,** 394; (e) D. Higgins, M. Hoque, M. Seo, R. Wang, F. Hassan, J. Choi, M. Pritzker, A. Yu, J. Zhang, Z. Chen, Adv. Fun. Mater., 2014, **24,** 4325.

8 J. Peng, W. Gao, B. Gupta, Z. Liu, R. Aburto, L, Ge, G. Song, L. Alemany, X. Zhan, G. Gao, S. Vithayathil, B. Kaipparettu, A. Marti, T. Hayashi, J. Zhu, P. Ajayan, Nano Lett., 2012, **12,** 844.

9 K. N. Kudin, B. Ozbas, H. C. Schniepp, R. K. Prud'homme, I. A. Aksay, R. Car, Nano Lett., 2008, **8,** 36.

10 H. Liu, Y. Liu, D. Zhu, J. Mater. Chem., 2011, **21,** 3335; L. Panchakarla, A. Govindaraj, C. Rao, ACS Nano, 2007, **1,** 494.

11 Z. Yang, Z. Yao, G. Li, G. Fang, H. Nie, Z. Liu, X. Zhou, X. Chen, S. Huang, ACS Nano, 2011, **6,** 205.

12 Y. Jiao, Y. Zheng, M. Jaroniec, S. Qiao, J. Am. Chem. Soc., 2014, **136,** 4394.

13 W. Gao, L. B. Alemany, L. J. Ci, P. M. Ajayan, Nat. Chem., 2009, **1,** 403.

14 K. Suenaga, and M. Koshino, Nature, 2010, **468,** 1088.

15 A. Thomas, A. Fischer, F. Goettmann, M. Antonietti, J. Müller, R. Schlögl, J. Carlssonc, J. Mater. Chem., 2008, **18**, 4893.

16 (a) M.A. Lukowski, A.S. Daniel, F. Meng, A. Forticaux, L. Li, S. Jin, J. Am. Chem. Soc., 2013, **135**, 10274; (b) W.F. Chen, C.H. Wang, K. Sasaki, N. Marinkovic, W. Xu, J. T. Muckerman, Y. Zhu, R. Adzic, Energy Environ. Sci., 2013, **6**, 943; (c) Y. Tan, P. Liu, L. Chen, W. Cong, Y. Ito, J. Han, X. Guo, Z. Tang, T. Fujita, A. Hirata, M. Chen, Adv. Mater., 2014, **26,** 8023; (d) Y. Zheng, Y. Jiao, Y. Zhu, L. Li, Y. Han, Y. Chen, A. Du, M. Jaroniec, S. Zhang Qiao, Nat. Commun., 2014, **5,** 3783; (e) Y. Zheng, Y. Jiao, L. Li, T. Xing, Y. Chen, M. Jaroniec, S. Zhang Qiao, ACS Nano, 2014, **8,** 5290; (f) Y. Zhao, F. Zhao, X. Wang, C. Xu, Z. Zhang, G. Shi, L. Qu, Angew. Chem. Int. Ed., 2014, **53,** 13934; (g) Y. Ito, W. Cong, T. Fujita, Z. Tang, M. Chen, Angew. Chem.

Int. Ed., 2015, **54,** 2131; (h) W. Cui, Q. Liu, N. Cheng, A. Asiricd, X. Sun, Chem. Commun., 2014, **50,** 9340.
17 Z. Chen, D. Cummins, B. N. Reinecke, E. Clark, M. K. Sunkara, T. F. Jaramillo, Nano Lett., 2011, **11,** 4168.
18 L. Liao, S. Wang, J. Xiao, X. Bian, Y. Zhang, M. Scanlon, X. Hu, Y. Tang, B. Liu and H. Girault, Energy Environ. Sci., 2014, **7,** 387
19 (a) J. Bonde, P. G. Moses, T. F. Jaramillo, J. K. Norskov, I. Chorkendorff, Faraday Discuss., 2008, **140,** 219; (b) T. F. Jaramillo, J. Bonde, J. Zhang, B. Ooi, K. Andersson, J. Ulstrup, I. Chorkendorff, J. Phys. Chem. C, 2008, **112,** 17492; (c) X. Zheng, J. Xu, K. Yan, H. Wang, Z. Wang, S. Yang, Chem. Mater., 2014, **26,** 2344.
20 L. P. Zhang, and Z. H. Xia, J. Phys. Chem. C, 2011, **115,** 11170.
21 R. Arsons, Trans. Faraday Soc., 1958, 1053.
22 J. Greeley, T. Jaramillo, J. Bonde, I. Chorkendorff, J. Nørskov, Nat. Mater., 2006, **5,** 909.
23 (a) S. Trasatti, Electroanal. Chem. Interfacial Electrochem., 1972, **39,** 163; (b) J. Greeley, L. Kibler, A. M. El-Aziz, D. M. Kolb, J. K. Nørskov, Chem. Phys. Chem., 2006, **7,** 1032; (c) M.C. Tavares, S.A.S. Machado, L.H. Mazo, Electrochim. Acta, 2001, **46,** 4359; (d) A. Chu and A. J. Sukava, J. Electrochem. Soc., 1969, **16,** 1188.
24 R. Subbaraman, D. Tripkovic, D. Strmcnik, K. Chang, M. Uchimura, A. Paulikas, V. Stamenkovic, N. Markovic, Science, 2011, **334,** 1256.

Graphical abstract

Electrocatalytic hydrogen evolution using graphitic carbon nitride coupled with nanoporous graphene co-doped by S and Se

S.S. Shinde, Abdul Sami, Jung-Ho Lee*

Department of Materials and Chemical Engineering, Hanyang University, Ansan, Kyunggido, 426-791, Republic of Korea